FLOW AND HEAT TRANSFER CHARACTERISTICS IN CHANNELS WITH PIRIFORM DIMPLES AND PROTRUSIONS

O. M. Oyewola [a,b,*], M. O. Petinrin[a], and H. O. Sanusi[a]

[a] *Department of Mechanical Engineering, University of Ibadan, Ibadan, Nigeria*
[b] *School of Mechanical Engineering, Fiji National University, Suva, Fiji*

ABSTRACT

The flow and heat transfer behaviour of channels with dimples and protrusions of spherical and piriform shapes was numerically explored by solving the Navier-Stokes and energy equations with a CFD software, the ANSYS Fluent 19.3, in the range of Reynolds numbers from 8,500 to 59,000. The values of the Nusselt number and friction factors were estimated and the non-dimensional Performance Evaluation Criterion (PEC) was determined to measure the thermal-hydraulic performance. The results reveal that the piriform protruded channel demonstrated a higher thermal performance with Nusselt number values of 36%, 15%, 23%, and 9% than the smooth, spherical dimpled, piriform dimpled, and spherical protruded channels, respectively. This indicates that heat transfer is enhanced by the turbulent mixing caused by the roughened surfaces of the channels. Nevertheless, the smooth channel had the lowest pressure drop with the friction factor of 20%, 7%, 21% and 27% less than that of spherical dimpled, piriform dimpled, spherical protruded, and piriform protruded channels, respectively. In the Reynolds number range, lower Nusselt number ratios and friction factor ratios were observed in the piriform dimpled channel compared to other enhanced-surface channels. The overall performance based on the thermal-hydraulic analysis indicated that the channel with piriform protrusions performed better with the highest PEC value of 3.77 times higher than the smooth-surface channel.

Keywords: *dimpled channel; protruded channel, piriform shape, heat transfer enhancement, friction factor*

1. INTRODUCTION

Highly effective heat transfer devices are becoming more and more preferred for various applications in thermodynamic systems, such as in the use of internally rough surface tubes to develop more compact and effective heat exchangers. This reduces energy usage and increases economic value. Among the best ways to boost heat transfer efficiency with a little pressure loss is to use the roughness enhancement approach (Wang et al., 2010). The goal of improving the rate of heat transfer while minimizing energy loss has led to extensive research into a number of heat transfer enhancement techniques like fins, ribs, and dimples in recent years (Turnow et al., 2012).

In many engineering applications, like the combustion chamber lining, gas turbine blades internal cooling, and minichannels cooling for mems devices, dimple/protrusion arrays are used to handle the high heat flux density (Li et al., 2020). They have also been widely employed to improve thermal device efficiency and performance in heat exchangers. In comparison to other heat transfer enhancement techniques, investigations have shown that dimpled and protruded surfaces can boost the heat transfer rate while producing very little pressure loss (Nascimento & Garcia, 2016; S. Wang et al., 2018).

A dimple is a small depression on a level surface that gives the impression of roughness. Spherical, teardrop and ellipsoidal dimpled geometries are only a few examples of dimpled geometries. The complex flow configurations that form over the dimple cavities have been studied in various ways. Dimples produce significant surface heat transfer enhancements with comparable lower pressure drop penalties than a number of other types of heat transfer enhancement surfaces, like the large-scale roughness and rib tabulators. This explains why manufacturers of different thermal fluid systems frequently incorporate them into the interior surfaces of channels (Won et al., 2015). Because vortex patterns encourage mixing, "cool" fluid from beyond the thermal boundary layer is pushed into contact with the wall, improving convective heat transfer over dimpled surfaces (Wang et al., 2018). Protruded surfaces are employed as a passive method of enhancing heat transfer by lowering the thermal resistance of the sublayer next to solid walls. It generates secondary flows, inhibits boundary layer growth, shear-layer reattachment, and recirculation, enhances mixing, and intensifies turbulence. Although this is not without the attendant pressure drop caused by the secondary flow losses, intense interactions between vortices and walls of the channel, and increased shear stresses and velocity gradients (Li et al., 2020).

Xie et al. (2018) carried out a numerical analysis of the heat transfer and flow characteristics in helically coiled mini-tubes with dimples to ascertain the impact of the dimples on heat transfer enhancement, flow patterns, and resistance behaviour. Three-dimensional Navier-Stokes equations with water as the working fluid were solved using the finite volume-based CFD code in the range of 500 to 6000 Reynolds numbers. Comparatively to a plain tube, the enhanced tube with protrusions and dimples has demonstrated an advantage for improved heat transfer rate using performance evaluation criteria (PEC). Jing et al. (2020) modelled channels having trapezoidal trailing edge with lateral slots and dimples on the end walls in various sizes and arrangements. The impacts of the channel orientation, the rotation number, and the arrangement of the dimples were explored. In stationary and rotational modes, wall heat transfer distributions, flow characteristics, and overall heat transfer performance were all numerically evaluated. Their findings

demonstrated that the channel orientation significantly impacted the flow and thermal performances. In study of Ratul et al. (2023), the effects of a dimpled surface over a minichannel heat exchanger on flow behaviour and heat transfer over a serpentine channel with a uniform rectangular cross-section were considered. Water and various volume concentrations of Al2O3-Cu/water nanofluid were used as coolants, and subjected to Reynolds number range of 5 x103 to 20 x 103. They recorded an improvement of 1.47 and 2.67-times in thermal efficiency using water and 1% vol. Al2O3-Cu/water nanofluid, respectively. Aasa et al. (2022a) conducted a numerical measurement of pressure drops and thermal transfer in rectangular ducts with four different compound angled dimples under the impact of mixed geometries with variable circular and oval dimple position and orientation angles. Their results had a great influence on the thermal performance of the dimpled rectangular channel. In another related study, Aasa et al. (2022b) Aasa etal2022b considered the arrangement and positions of dimples of three geometrical aspect ratios (depth-to-print diameter ratios) of 0.050 - circular, 0.035 - oval, and 0.025 – oval, at a pitch-to-depth ratio of 6. Their study revealed an influence of the compound arrangement on the thermal-hydraulic performance of the system with the best at 0.025 aspect ratio.

Leontiev et al. (2017) performed an experiment to assess the relative drag and coefficient of heat transfer of several dimpled surface shapes, which included spherical, rounded-edged spherical, oval, teardrop, and turned teardrop dimples. Their research revealed that the dimples with sphere and rounded sides has the highest thermal-flow performance. Wang et al. (2010) experimentally investigated the design of a compact, highly effective heat exchanger with improved dimpled tubes from ellipsoidal and spherical protrusions. The efficiency of protruded tubes is superior to that of smooth tubes. Their results indicated a higher Nusselt number to friction factor ratio for the ellipsoidal dimpled tube. Farsad et al. (2022) carried out a numerical analysis of turbulent forced convective fluid transport of water in dimpled-protruded tubes. They observed an increase in interfacial heat transfer, which they attributed to vortices at the locations of the combined dimples and protrusion. They also discovered an insignificant frictional effect when compared to the gain in heat transfer. Li et al. (2020) investigated the flow patterns and improvements in heat transfer in rectangular ducts with protrusions and dimples in the range of Reynolds number between 5600 and 22,000. Comparisons on the impact of the distance of roughness elements with varying Reynolds number were carried out. Their findings demonstrated that decrease in the gap ratio with increasing the Reynolds number significantly improved thermal performance, however, the flow structure case is exclusively connected to the Reynolds number. Khan et al. (2021) introduced dimple-protrusion surfaces into rectangular cross-section channel to understand the thermal characteristics of water-based CuO nanofluid through the channel in the laminar flow regime. They found an average of 10% improvement in thermal performance over straight rectangular cross-section channel.

On the basis of earlier investigations and reviewed literature, it is evident that adding dimples and protrusions to the flow channel's surface has significantly improved the channel's thermal and hydraulic performance relative to plain or smooth channels. However, there is a paucity of literature on channels with piriform-shaped dimples and protrusions, despite the fact that studies have shown that the shapes of the dimples and protrusions have a significant impact on the thermal and flow properties of the channels. The purpose of this numerical study is to compare the performance of piriform channels with dimpled and protruded surfaces of piriform shapes to channels with smooth and spherical dimpled and protruded surfaces. The knowledge of this investigation will improve our understanding on the response of large scale structure to surface modification of these types for proper heat transfer enhancement and applications.

2. METHODOLOGY

2.1 Geometry of the Model

Different layouts of a rectangular channel with and without roughened surfaces are subjected to three-dimensional simulation. Roughness in form of protrusions and dimples is created on the test section's bottom wall. The dimpled test section has a width of 130 mm, and a total length of 245 mm. Fig. 1 shows the schematic representation of the dimple or protrusion arrangement on a test plate within a channel as obtained from Rao et al. (2015).
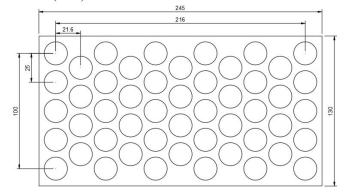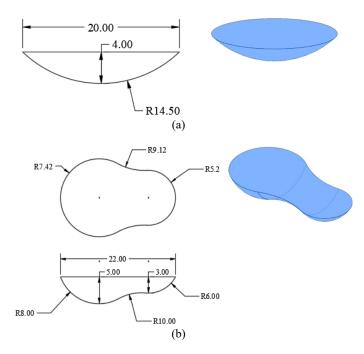

Fig. 1. Arrangement of dimples/protrusions in the test section

The geometrical dimensions of each of the spherical and piriform dimple configurations are as described in Fig. 2. The print diameter of the spherical dimples is 20 mm with depth of 4 mm. Protrusions are of the same dimensions as the dimples but are embossed on the test plate. The piriform dimples/protrusions were created to have approximately the same scoop volume or embossed volume as the spherical dimples/protrusions. The transverse spacing-to-diameter ratio of the dimple/protrusion arrangement is 1.25, while the streamwise spacing-diameter ratio is 1.08.

Fig. 2. The geometrical dimensions of the dimples (a) spherical dimple (b) piriform dimple

2.2 Governing Equations

This study makes use of the CFD code, Fluent version 19.3, which employs the finite volume technique to solving the governing equation. The following are the underlying governing equations for a steady state and an incompressible flow condition (Pletcher et al., 2013):

Continuity equation;

$$\frac{\partial u_i}{\partial x_i} = 0 \tag{1}$$

Momentum conservation equation;

$$\rho \frac{\partial}{\partial x_j}(u_i u_j) = -\frac{\partial p}{\partial x_i} + \frac{\partial}{\partial x_j}(\mu + \mu_t)\left(\frac{\partial u_i}{\partial x_j} + \frac{\partial u_j}{\partial x_i}\right) - \frac{2}{3}\rho k \delta_{ij} \tag{2}$$

Energy conservation equation;

$$\rho \frac{\partial}{\partial x_i}(u_i T) = \frac{\partial}{\partial x_i}\left[\left(\frac{\mu}{Pr} + \frac{\mu_t}{Pr_t}\right)\frac{\partial T}{\partial x_i}\right] \tag{3}$$

where ρ is the fluid density, p is pressure, T is temperature, Pr is the Prandtl number, μ_t is turbulent viscosity, μ is dynamic viscosity, and u_i is the velocity vector.

The realizable k-ε turbulence model is used to model the governing equations with extra transport equations as presented in equations (4) and (5) (Shih et al., 1995):

Turbulence kinetic energy (k) equation;

$$\frac{\partial}{\partial x_j}(\rho k u_j) = \frac{\partial}{\partial x_j}\left[\left(\mu + \frac{\mu_t}{\sigma_k}\right)\frac{\partial k}{\partial x_j}\right] + \Gamma - \rho\varepsilon \tag{4}$$

Turbulent dissipation rate (ε) equation;

$$\frac{\partial}{\partial x_j}(\rho\varepsilon u_j) = \frac{\partial}{\partial x_j}\left[\left(\mu + \frac{\mu_t}{\sigma_\varepsilon}\right)\frac{\partial\varepsilon}{\partial x_j}\right] + \rho C_1 S\varepsilon - C_2\frac{\varepsilon^2}{k+\sqrt{v\varepsilon}} \tag{5}$$

where the production term, Γ is expressed as follows:

$$\Gamma = -\overline{u_i u_j}\frac{\partial u_i}{\partial u_j} = \left[\mu_t\left(\frac{\partial u_i}{\partial x_j} + \frac{\partial u_j}{\partial x_i}\right) - \frac{2}{3}\rho k \delta_{ij}\right]\frac{\partial u_i}{\partial x_j} \tag{6}$$

Other parameters are:

$$C_1 = max\left[0.43\frac{\mu_t}{\mu_t + 5}\right]$$

where $\mu_t = S\frac{k}{\varepsilon}, S = \sqrt{2S_{ij}S_{ij}}$ and model constants; $C_{\varepsilon 1} = 1.44, C_2 = 1.9, \sigma_k = 1.0, \sigma_\varepsilon = 1.2$

$$\mu_t = \rho C_\mu \frac{k^2}{\varepsilon}$$

$$where \ C_\mu = \frac{1}{A_o + A_s\frac{kU^*}{\varepsilon}}$$

$$U^* = \sqrt{S_{ij}S_{ij} + \widetilde{\Omega}_{ij}\widetilde{\Omega}_{ij}}$$

$$\widetilde{\Omega}_{ij} = \Omega_{ij} - 2\epsilon_{ijk}w_k; \ \Omega_{ij} = \widetilde{\Omega}_{ij} - \epsilon_{ijk}w_k$$

where the mean rate-of-rotation tensor, $\widetilde{\Omega}_{ij}$ is viewed with angular velocity w_k in a moving reference frame.

The model constants A_s and A_o are given by:

$$A_s = \sqrt{6}\cos\psi, \qquad A_o = 4.04$$

where,

$$\psi = \frac{1}{3}\cos^{-1}\sqrt{6}W, \qquad W = \frac{S_{ij}S_{jk}S_{ki}}{S^3},$$

$$S = \sqrt{S_{ij}S_{ij}}, \quad S_{ij} = \frac{1}{2}\left(\frac{\partial u_i}{\partial x_j} + \frac{\partial u_j}{\partial x_i}\right)$$

2.3 Boundary Conditions

The boundary condition schematic is shown in Fig. 3. Reduced channel geometry was used to save computational costs, and only a span-wise periodic dimpled channel section was examined under the assumption that the channel flow had periodic boundary conditions. The figure depicts the test section's fluid domain for both the spherical and piriform dimpled test channel, which is 25 mm wide and 20 mm high. The bottom wall of the dimpled section was heated to a uniform temperature of 318.15 K (45ºC), while the top wall was insulated. The other walls of the channel were kept adiabatic, that is, at zero heat flux. The above and below surfaces of the dimpled section are handled as no-slip boundaries. A supplemental length of smooth channel of 240 mm is employed

upstream and downstream of the test domain. Before reaching the dimpled test section, the flow is considered to be completely developed at the adiabatic inlet part of the channel.

Air serves as the working fluid, and the channel is composed of copper. The fluid and channel thermo-physical properties were assumed constant. The channel inlet and exit were prescribed as velocity inlet and pressure outlet boundary conditions, respectively. The initial velocity and pressure were set to zero, and the fluid temperature to 300 K as the initial conditions. The inlet temperature was maintained at 300 K. Zero gauge pressure and zero gradients for the primitive variables were given at the outflow boundary.
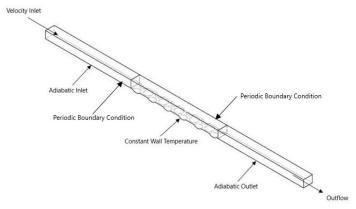

Fig. 3. Boundary conditions for the dimpled channel

2.4 Numerical Setup

The ANSYS Fluent 19.3 is the code utilized for numerical simulation and solving the momentum and energy equations. The momentum, pressure-based continuity equations, and the two k-ε equations are all solved using the coupled technique. The second-order upwind was employed for velocity and pressure while first-order upwind was used for the turbulent kinetic energy and dissipation rate. The scale residual has convergence conditions of the order of 10^{-6} for energy parameters and 10^{-5} for velocity and continuity parameters. To initialise the velocity and temperature fields in the computational domain, the hybrid initialisation method was used.

The sizing method was used to create high-quality mesh across the entire domain. The domain was body sized with an element size of 1 mm and a growth rate of 1.2, with 181,213 nodes and 516,497 elements and medium smoothing. Quadrilateral and hexagonal mesh components were used to mesh the fluid domain. On the fluid domain, average orthogonal quality of 0.8298 and skewness of 0.16924 were maintained. Fig. 4 shows an illustration of the structured mesh over the domain
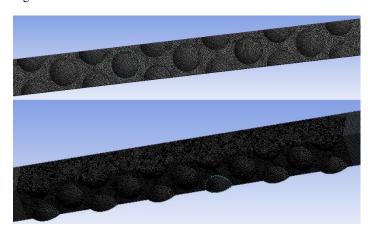

Fig. 4. Structured mesh around dimpled section

2.5   Grid Independence Analysis

To ensure that the number of cells does not significantly affect the solution, a grid independence analysis was performed. Four grid schemes with the element numbers 199,624, 305,935, 516,497, and 631,153, respectively, were created to determine the Nusselt number as listed in Table 1. In contrast to the differences between other schemes, the Nusselt number difference between the grid systems of schemes 4 and 5 is substantially less. Consequently, the grid system with 516,497 element numbers was chosen for this investigation to balance computational economy and prediction accuracy while minimising the use of computer resources.

Table 1: Grid Independence Analysis

Numerical Schemes	Element No.	Nu	% diff.
1	199624	65.23	-
2	305935	79.63	21.5
3	516497	90.14	14.1
4	631153	91.52	1.5

2.6   Data Reduction

It is critical to get the flow and thermal field characteristics in order to calculate the friction factor, Nusselt number, and thermal-hydraulic performance. The dimpled channels' averaged coefficient of heat transfer of the wetted-area is given as (Bergman et al., 2011):

$$h = \frac{\dot{Q}_{net}}{A_{wet}\Delta T_{lm}} \quad (7)$$

where Q_{net} is the net heating rate and it is defined by:

$$\dot{Q}_{net} = \dot{m}C_p(T_{out} - T_{in}) \quad (8)$$

A_{wet} is the total area of the wetted surface of the dimples, and ΔT_{lm}, which is the log mean temperature difference, is given by:

$$\Delta T_{lm} = \frac{(T_w - T_{in}) - (T_w - T_{out})}{\ln(\frac{T_w - T_{in}}{T_w - T_{out}})} \quad (9)$$

The average Nusselt number is used to characterize heat transfer performance, and it is given as

$$\overline{Nu} = \frac{hD_h}{\lambda} \quad (10)$$

where λ is the fluid's thermal conductivity, h is the coefficient of heat transfer and D_h is the channel's hydraulic diameter, and the formula is as follows:

$$D_h = \frac{4A_c}{P} \quad (11)$$

where A_c is the cross-sectional area of the channel and P_w is the wetted perimeter.

The Darcy friction factor is used to characterise the flow resistance of a flow over a dimpled channel; the following formula is used to compute it (Bergman et al., 2011; Holman, 2010):

$$f = \frac{\Delta p}{\left[(L/D_h)(1/2\rho u^2)\right]} \quad (12)$$

where the pressure drop of airflow over the test channel is Δp, the average velocity in the test channel is u, and the length of the test channel is L, which is 245 mm.

The performance evaluation criteria (PEC) factor measures the improvement in overall thermal-hydraulic performance caused by passive enhancing techniques, and it is calculated as follows (Li et al., 2020; Moradi et al., 2023):

$$PEC = \frac{Nu/Nu_o}{(f/f_o)^{1/3}} \quad (13)$$

3.   RESULTS AND DISCUSSION

3.1   Validation of the model

A comparison was made between the predictions in this work and the findings of an experiment work of Rao et al. (2015) to validate the present numerical solution of dimpled/protruded channel flow. Fig. 5 shows the

range the range Nusselt numbers against the friction factors obtained for the smooth dimpled channel for both cases. It is clearly shown that the numerical and experimental results correlate well. Although there is variation in the Nusselt number and friction factor obtained from this study with an error of 17.09% and 13.48% respectively. The slight deviation could be ascribed to the simplification of the geometrical model and choice of numerical schemes.
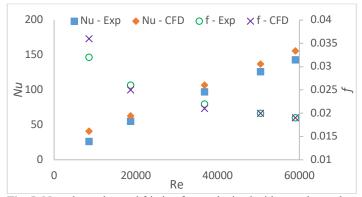

Fig. 5: Nusselt number and friction factor obtained with experimental data
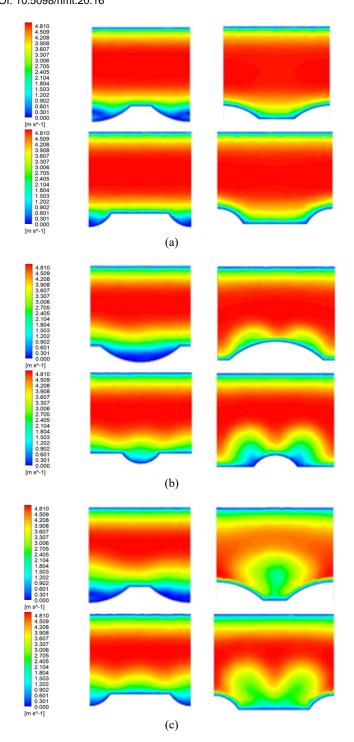
3.2   Velocity distribution

Fig. 6 shows the distribution of velocity in transverse sections at 20.0 mm, 122.5 mm, and 230.0 mm into the spherical-dimpled, spherical-protruded, piriform-dimpled, and piriform-protruded plates at a Reynolds number of 8,500. It is evident that the flow velocity increases at contraction regions of dimpled/protruded sections. As the protrusions cause an obstruction to the flow, the fluid velocity tends to increase at the contracted flow area to keep the law of conservation of mass. However, the velocity increases in the sections without dimples but reduces in dimpled sections. These observations become more pronounced as the fluid flows through the channel at 20.0 mm, 122.5 mm, and 230.0 mm into the dimpled/protruded sections. This contraction and enlargement along the flow path contribute to a more heat transfer interaction at the heaps of the dimpled/protruded sections than for the plane channel.

3.3   Turbulent Kinetic Energy

Fig. 7 compares the turbulent kinetic energy in the bottom plate with various protrusion and dimple surfaces for Re = 8,500. It is obvious that all of the channels with dimples experienced an increase in turbulent mixing on the leeward side of the dimples as a result of the vortex flows induced from the dimples while in the protruded channels, there was enhanced turbulent mixing in the windward side caused by the protrusions. Thus, rate of heat transfer is enhanced at these regions of turbulent mixing than in the recirculation zones closest to the leading edge within the dimples and the leeward sides of the protrusions.
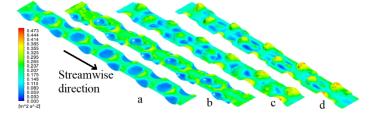
3.4   Heat Transfer

Comparison The coefficient of heat transfer of the smooth, spherical dimpled, piriform dimpled channels spherical protruded, and piriform protruded channels over the Reynolds number range, 8,500 – 59,000, is presented in Fig. 8. As the Reynolds number rises, the average heat transfer coefficient of piriform protruded channels is larger than that of smooth, spherical dimpled, piriform dimpled and spherical protruded channels. The Nusselt number of smooth, spherical dimpled, piriform dimpled, spherical protruded, and piriform protruded channels are compared in Fig. 9.

Fig. 6. Velocity plots at transverse cross-sections of spherical-dimpled, spherical-protruded, piriform-dimpled, and piriform-protruded channels (a) 20.0 mm, (a) 122.5 mm, and (c) 230.0 mm of the dimpled/protruded section

It can be deduced that the increase in Reynolds number of flow through the channels causes the rise Nusselt number. As depicted in Fig. 9, the Nusselt number for the piriform protruded channel ranges from 62.0 to 167.5, which is in the range of Reynold number, 1.46 times that of the smooth channel, 1.14 times that of the spherical dimpled channel, 1.27 times that of the piriform dimpled channel and 1.09 times that of the spherical protruded channel. In comparison to the piriform protruded channel, the Nusselt number values for the smooth, spherical dimpled,

piriform dimpled, and spherical protruded channels are averagely lower by 36%, 15%, 23%, and 9%, respectively. As a result, the heat transfer performance of the piriform protruded channel is the best of all the cases studied. Fig. 10 illustrates the comparison of the Nusselt numbers of the dimpled and protruded channels when compared to that of the smooth channel. Hence, the piriform protruded channel has the best heat transfer performance of all the dimpled and protruded channels.

Fig. 7. Turbulent Kinetic Energy (TKE) Distributions for the various dimpled and protruded channels at Re = 8,500
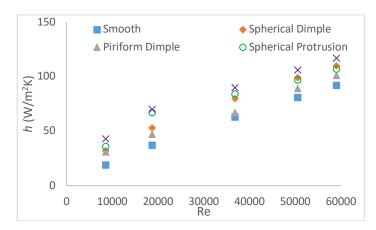

Fig. 8. Heat Transfer Coefficient of test channels
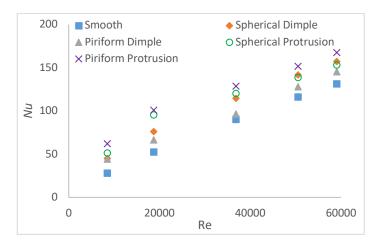

Fig. 9. Nusselt numbers of test channels

3.5 Flow friction

The numerical approach was used to obtain the flow characteristics of fluid in the test sections within the Reynolds number range of 8,500 to 59,000. To facilitate comparison, the smooth channel's friction factor was also obtained within the same Reynolds number range. Fig. 11 shows the friction factors of the test channels. The friction factor reduces with increase in the Reynolds number, as shown in Fig. 11. The smooth

channel has the lowest pressure drop with the friction factor of 20%, 7%, 21% and 27% less than that of spherical dimpled, piriform dimpled, spherical protruded, piriform protruded channels, respectively. The normalised friction factor, which is the ratio of the flow friction factor in any of the roughened channels to the corresponding values at the same Reynolds number in the smooth channel is presented in Fig. 12. It could be observed from this figure that the spherical dimpled, piriform dimpled, spherical protruded, piriform protruded channels exhibited higher friction factor at the ratios by 1.21, 1.08, 1.22, and 1.28, respectively. Thus, the piriform protruded channel loses the most pressure owing to flow friction, whereas the piriform dimpled channel has the best hydraulic performance of all the dimpled and protruded channels.
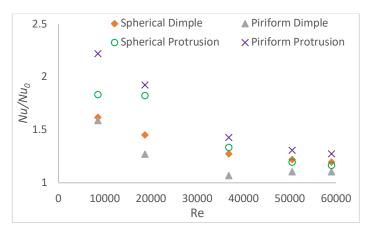

Fig. 10. Nusselt number ratios of the dimpled and protruded channels
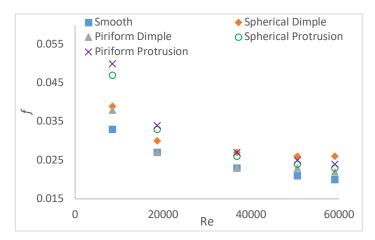

Fig. 11. Friction factors of the test channels

3.6 Thermal-Hydraulic Performance

Only after accounting for the penalty effects associated with pressure losses can the thermal performance of the test channels be adequately assessed. To characterise the thermal-hydraulic performance of the dimpled and protruded channels, a criterion known as the Performance Evaluation Criteria (PEC) is used, as illustrated in Fig. 13. As clearly indicated from this figure, the thermal-hydraulic performance of the dimpled and protruded surfaces is higher than that of the smooth surface channel with the *PEC* of not less than 2.7 at Re = 59,000, indicating that the pressure drop penalty caused by enhanced surfaces dominates the performance in higher Reynold number regions. Apparently from the figure, the overall performance demonstrated by the spherical dimpled, piriform dimpled, spherical protruded, and piriform protruded channels are averagely 3.38, 3.41, 3.58, and 3.77 times higher than the

corresponding value for the smooth channel, respectively. As a result, the protruded channels' performance could be attributed to the turbulent mixing that is enhanced by the presence of vortex structures associated with the heaps of the protruded surfaces, especially the double heaps from the piriform protrusions.

The piriform protruded channel has the highest average thermal-hydraulic performance, which is about 12%, 11% and 5% greater than that of the spherical dimpled channel, piriform dimpled and spherical protruded respectively as shown in Fig. 13.
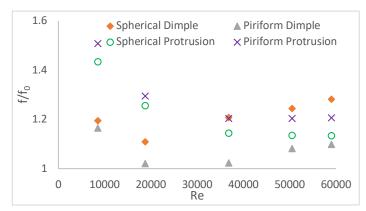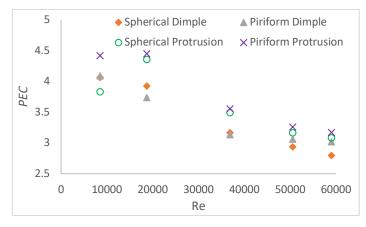

Fig. 12. Normalised friction factor of the dimpled and protruded channels

Fig. 13. Overall thermal performance of the dimpled and protruded channels

4. CONCLUSIONS

The flow and heat transfer in smooth, spherical dimpled, piriform dimpled, spherical protruded, and piriform protruded channels was carried out numerically in this study. For each of the test channels, heat transfer enhancement, flow resistance, and overall thermal performance were evaluated and compared for the Reynolds number range of 8,500 to 59,000. The findings indicated that they greatly influenced the thermal and flow characteristics of the channels. The results revealed that the piriform protruded channel demonstrated a higher thermal performance with Nusselt number values of 36%, 15%, 23%, and 9% than the smooth, spherical dimpled, piriform dimpled, and spherical protruded channels, respectively. While the pressure drop recorded for the smooth channel is the lowest, the piriform protruded channel had the best heat transfer characteristic although with a very high pressure penalty as compared with others. It was the most effective in terms of heat transfer augmentation. The piriform dimpled channel was the most effective in terms of hydraulic performance among the enhanced-surface channel

with relatively lower pressure loss but relatively low heat transfer performance. In all, the piriform protruded channel has the best overall thermal-hydraulic performance.

NOMENCLATURE

Abbreviations and Symbols

Re	Reynolds Number;
u	Velocity, m/s;
D_h	Hydraulic Diameter, m;
p	Pressure, Pa;
T	Temperature, K;
Pr	Prandtl Number;
k	Turbulence Kinetic Energy, m^2/s^2;
C_p	Specific heat capacity at constant pressure, J/kg.K;
h	Heat Transfer Coefficient, W/m^2K;
Q	Total Heat, J;
A_{wet}	Wetted Area of dimpled surface, m^2;
ΔT_{lm}	Log Mean Temperature Difference, K;
Nu	Nusselt Number;
P	Wetted Perimeter, m.

Greek Symbols

ρ	Density, kg/m^3;
λ	Thermal Conductivity, W/m.K;
μ	Dynamic Viscosity, kg/ms;
μ_t	Turbulent Eddy Viscosity, kg/ms;
ε	Specific Dissipation Rate, m^2/s.

Subscripts

i,j	Indexes of vectors;
in	inside;
out	outside;
w	wall.

REFERENCES

Aasa, S. A., Shote, A. S., Giwa, S. O., and Sharifpur, M. 2022a, "Convective thermohydraulic heat transfer enhancement of mixed dimpled geometries in rectangular channel," *Fuel Communications*, *10*, 100044. https://doi.org/10.1016/j.jfueco.2021.100044

Aasa, S. A., Shote, A. S., Giwa, S. O., and Sharifpur, M. 2022b, "Friction factor effect and heat transfer enhancement in combined dimple geometry arrange in different angle to flow direction," *Fuel Communications*, *10*, 100043. https://doi.org/10.1016/j.jfueco.2021.100043

Bergman, T. L., Lavine, A. S., Incropera, F. P., and Dewitt, D. P. 2011, *Fundamentals of heat and mass transfer* (7th ed.). John Wiley and Sons.

Farsad, S., Mashayekhi, M., Zolfagharnasab, M. H., Lakhi, M., Farhani, F., Zareinia, K., and Okati, V. 2022, "The effects of tube Dimples-Protrusions on the thermo-fluidic properties of turbulent forced-convection," *Case Studies in Thermal Engineering*, *35*, 102033. https://doi.org/10.1016/j.csite.2022.102033

Holman, J. P. 2010, *Heat Transfer* (10th ed.). McGraw-Hill.

Jing, Q., Xie, Y., and Zhang, D. 2020, "Numerical investigation of flow and heat transfer in rotating trapezoidal channel with lateral slots and dimple structure," *International Communications in Heat and Mass Transfer*, *118*, 104865. https://doi.org/10.1016/j.icheatmasstransfer.2020.104865

Khan, M. Z. U., Akbar, B., Sajjad, R., Rajput, U. A., Mastoi, S., Uddin, E., Hussain, A., Younis, M. Y., García Márquez, F. P., and Akram, N. 2021, "Investigation of heat transfer in dimple-protrusion micro-channel

heat sinks using copper oxide nano-additives," *Case Studies in Thermal Engineering*, *28*. https://doi.org/10.1016/j.csite.2021.101374

Leontiev, A. I., Kiselev, N. A., Vinogradov, Y. A., Strongin, M. M., Zditovets, A. G., and Burtsev, S. A. 2017, "Experimental investigation of heat transfer and drag on surfaces coated with dimples of different shape," *International Journal of Thermal Sciences*, *118*, 152–167. https://doi.org/10.1016/j.ijthermalsci.2017.04.027

Li, M., Chen, X., and Ruan, X. 2020, "Investigation of flow structure and heat transfer enhancement in rectangular channels with dimples and protrusions using large eddy simulation," *International Journal of Thermal Sciences*, *149*(January 2019), 106207. https://doi.org/10.1016/j.ijthermalsci.2019.106207

Moradi, T., Shahbazian, H., Hoseinalipour, M., and Sunden, B. 2023, "Effects of wavy ribs on vortex generation and thermal-hydraulic performance in a rotating rectangular channel," *Applied Thermal Engineering*, *222*, 119952. https://doi.org/10.1016/j.applthermaleng.2022.119952

Nascimento, I. P., and Garcia, E. C. 2016, "Heat transfer performance enhancement in compact heat exchangers by using shallow square dimples in flat tubes," *Applied Thermal Engineering*, *96*, 659–670. https://doi.org/10.1016/j.applthermaleng.2015.11.042

Pletcher, R. H., Tannehill, J. C., and Anderson, D. A. 2013, *Computational fluid mechanics and heat transfer* (3rd ed.). CRC Press, Taylor & Francis Group.

Rao, Y., Feng, Y., Li, B., and Weigand, B. 2015, "Experimental and numerical study of heat transfer and flow friction in channels with dimples of different shapes." *Journal of Heat Transfer*, *137*(031901), 1–10. https://doi.org/10.1115/1.4029036

Rao, Y., Li, B., and Feng, Y. 2015, "Heat transfer of turbulent flow over surfaces with spherical dimples and teardrop dimples," *Experimental Thermal and Fluid Science*, *61*, 201–209. https://doi.org/10.1016/j.expthermflusci.2014.10.030

Ratul, R. E., Ahmed, F., Alam, S., Rezwanul Karim, M., and Bhuiyan, A. A. 2023, "Numerical study of turbulent flow and heat transfer in a novel design of serpentine channel coupled with D-shaped jaggedness using hybrid nanofluid," *Alexandria Engineering Journal*, *68*, 647–663. https://doi.org/10.1016/j.aej.2023.01.061

Shih, T.-H., Liou, W. W., Shabbir, A., Yang, Z., and Zhu, J. 1995, "A new k-e eddy viscosity model for high reynolds number turbulent flows - model development and validation," *NASA Technical Memorandum*, *24*(3), 227–238.

Turnow, J., Kornev, N., Zhdanov, V., and Hassel, E. 2012, "Flow structures and heat transfer on dimples in a staggered arrangement," *International Journal of Heat and Fluid Flow*, *35*, 168–175. https://doi.org/10.1016/j.ijheatfluidflow.2012.01.002

Wang, S., Du, W., Luo, L., Qiu, D., Zhang, X., and Li, S. 2018, "Flow structure and heat transfer characteristics of a dimpled wedge channel with a bleed hole in dimple at different orientations and locations," *International Journal of Heat and Mass Transfer*, *117*, 1216–1230. https://doi.org/10.1016/j.ijheatmasstransfer.2017.10.087

Wang, Y., He, Y., Lei, Y., and Zhang, J. 2010, "Heat transfer and hydrodynamics analysis of a novel dimpled tube," *Experimental Thermal and Fluid Science*, *34*(8), 1273–1281. https://doi.org/10.1016/j.expthermflusci.2010.05.008

Won, S. Y., Ligrani, P. M., and Lee, J. G. 2015, "Numerical analysis of flow structure above dimpled surfaces with different depths in a channel," *Numerical Heat Transfer; Part A: Applications*, *67*(8), 827–838. https://doi.org/10.1080/10407782.2014.949198

Xie, S., Liang, Z., Zhang, L., Wang, Y., Ding, H., and Zhang, J. 2018, "Numerical investigation on heat transfer performance and flow characteristics in enhanced tube with dimples and protrusions," *International Journal of Heat and Mass Transfer*, *122*, 602–613. https://doi.org/10.1016/j.ijheatmasstransfer.2018.01.106